ACS APPLIED MATERIALS & INTERFACES

Research Article

www.acsami.org

Hydrothermally Grown Upright-Standing Nanoporous Nanosheets of Iodine-Doped ZnO (ZnO:I) Nanocrystallites for a High-Efficiency Dye-Sensitized Solar Cell

Khalid Mahmood,[†,‡] Hyun Wook Kang,[‡] Seung Bin Park,[†,*] and Hyung Jin Sung[‡]

[†]Department of Chemical & Biomolecular Engineering and [‡]Department of Mechanical Engineering, Korea Advanced Institute of Science and Technology, 291 Daehak-ro, Yuseong-gu, Daejeon, 305-701, Republic of Korea

ABSTRACT: Upright-standing nanoporous nanosheets of iodine-doped ZnO (ZnO:I) nanocrsytallites were grown hydrothermally at low temperature and studied as dye-sensitized solar-cell electrodes. The highest overall energy-conversion efficiency of ~6.6% was achieved with the film consisted of nanosheets of ZnO:I nanocrystallites. This efficiency was significantly improved than the 3.2% achieved for ZnO:I films only including nanosized crystallites, and higher than the 2.4% for undoped ZnO nanosheet film. The nanosheets of ZnO:I nanocrsytallites were proven to be positive in causing light scattering in a broad wavelength region and, therefore, enhancing the light harvesting capability of the photoelectrode film and thus, promotes the solar cell performance. The fabricated cells exhibited highly durable cell performances, even after a month under atmospheric conditions. Electrochemical impedance spectroscopy (EIS) data confirmed that iodine doping was helpful to lower the recombination resistance and prolonged electron lifetime of the ZnO:I cells, hence diminishing the recombination process. The efficiency achieved for the best DSSC in this work was much better than ever reported for a ZnO-based DSSC.

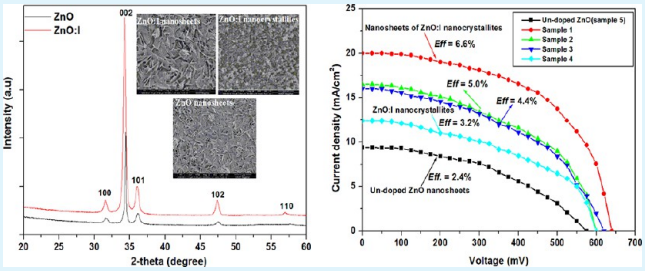

KEYWORDS: *ZnO nanosheets, nanocrystalline, dye-sensitized solar cell, hydrothermal, light scattering*

1. INTRODUCTION

Dye-sensitized solar cells (DSSCs) have been promising for the conversion of solar energy to electricity because of their easy manufacturing process, low fabrication cost, and relatively high efficiency.[1] The idea of DSSCs is based on the optical excitation of a dye that injects an electron into the conduction band of a wide band gap nanostructured metal oxide. The oxidized dye molecule is afterward regenerated back to its ground state by gaining one electron from a redox couple that is found in an electrolyte around the sensitized metal oxide nanostructured film. The transport of charge carriers and light harvesting are thus separated by using a suitable combination of three materials: metal oxide, dye, and electrolyte.[2] Currently, the primary photovoltaic (PV) material for DSSCs is titanium dioxide (TiO_2), for which the considerable power conversion efficiency of 12.3% have been successfully accomplished.[3] In contrast, other metal oxide semiconductors such as zinc and tin oxides, have received less attention even of these materials have the comparable band gap widths and photoelectrochemical properties to TiO_2.[4−8] Zinc oxide (ZnO) has higher electron mobility (~205−1000 $cm^2\ V^{-1}\ s^{-1}$) than TiO_2 (~0.1− 4 $cm^2\ V^{-1}\ s^{-1}$), enabling faster diffusion transport of photoinjected electrons when it is used as the electrode material in DSSCs.[9] In addition, ZnO is a convenient material for the mesoporous electrode in DSSCs, which has a band gap of 3.2 eV and a conduction band edge position of −4.3 eV, both of which are similar to TiO_2.[2] Moreover, ZnO can be easily processed into various nanostructures, such as nanoparticles,[10] nanowires,[5,6] nanotubes,[4] and tetrapods,[11] providing numerous alternatives for optimizing the electrode morphology so as to enhance the charge collection. However, the conversion efficiency of ZnO-based DSSCs reported so far still remains lower than those fabricated from TiO_2, leaving plenty of room to improve the efficiency through structural and morphology modification of the electrode.

Competition between the generation and recombination of photoexcited carriers in DSSCs is a main obstacle for developing higher conversion efficiency.[12] One possible solution is to use one-dimensional (1D) nanostructures that are able to support a direct pathway for the rapid collection of photogenerated electrons and, hence, reduce the degree of charge recombination.[13−16] However, such 1D nanostructures seem to have insufficient internal surface area, which limits their energy conversion efficiency to a relatively low level, for example, 1.5% for ZnO nanowires[13] and 4.7% for TiO_2 nanotubes.[15] Another way to increase efficiency is to increase

Received: December 28, 2012
Accepted: March 19, 2013
Published: March 19, 2013

the light-harvesting capability of the photoelectrode film by utilizing optical enhancement effects, which can be accomplished by light scattering by means of scatterers installed into the photoelectrode film. It is well-known that nanoporous TiO_2 film that was reported by Gr̈atzel and co-workers[17,18] can lead to very high solar-to-electric energy conversion efficiency (above 10%). Therefore, the preparation of nanoporous ZnO film is also a key to improve the performance of ZnO-based DSSCs. In addition, hierarchical structure of ZnO aggregates, composed of submicrometer sized crystallites can be used as efficient light scatters, offering relatively large specific surface area framework, and removing the adverse effect caused by the lowered adsorption of dye-molecules in the film. For the case of employing the polydisperse aggregation of ZnO nanocrystallites, an overall energy-conversion efficiency of up to 5.4% has been achieved.[19] In addition, an unprecedented photoconversion efficiency of 7.5% for ZnO-based DSSCs was achieved for a photoelectrode consisting of polydispersed ZnO aggregates of nanocrystallites over a compact ZnO buffer layer at a firing temperature of 450 °C.[20] However, the drawback was that the nanoporous films and employment of these particles into nanocrystalline films will inevitably lower the internal surface area of the photoelectrode film and, thus, counteract the enhancement effect of light scattering on the optical absorption, which in turn will increase the recombination rate of photogenerated carriers. On the other hand, either poor injection and/or strong recombination are indeed responsible for the limited performance of ZnO nanowire arrays in a DSSC. It was reported that vertically aligned ZnO nanowire arrays sensitized with highly absorbing dyes can reach good solar light harvesting in spite of the low surface area, but care should be taken to control recombination and electron losses from the substrate.[21]

Particularly, ZnO nanosheets are quasi-two-dimensional structures for which the performance of the solar cell is also believed to benefit from a high degree of crystallinity, larger surface area and, therefore, low resistance with regards to electron transport. To achieve these characteristics, the two-dimensional (2D) ZnO nanosheets have been investigated as the photoanodes of DSSCs.[22−26] Hosono et al. studied the chemical bath deposition method for the preparation of DSSC based on ZnO porous nanosheets. However, the cells exhibited an efficiency of only 3.9% because of the lower surface area for the adsorption of dye.[27] Xu et al. used the electrodeposited ZnO nanosheets for the preparation of the photoanode of a DSSC,[28] but the cell showed an efficiency of only 2.3%; this cell efficiency was limited because of a low surface area for dye adsorption and as well as the high thickness of nanosheets. In addition, the best energy-conversion efficiency (η) obtained with a mosaic structure composed of ZnO nanosheets was 5.41%.[23] In the case of aforementioned studies, film deposition methods like chemical bath deposition, doctor-blade, and electrodeposition were utilized with difficulty of operation, varying degrees of expenses, and sophistication to fabricate the thin films of ZnO nanosheets. The presented two-step method has many advantages such as low cost, environmental friendliness, scalability, and its applicability to a variety of substrates such as silicon, sapphire, and glass. In addition, the improved control over the morphology by means of different conditions (chemicals selection, precursor concentration, growth time, and synthesis temperature) is the key benefit of this process. Typically, visible response of ZnO nanomaterials can be realized by doping nonmetal elements such as N, S, and C, as previously reported for the photocatalytic degradation of pollutants and photoelectrochemical water splitting, where ZnO was used as the photocatalysts.[29,30] The non-metal-doping not only narrows the band gap so as to be responsible for visible light, but also inhibits the recombination of photogenerated electrons and holes.[30] Combination of all these features will likely produce higher efficiency for ZnO-based DSSCs.

In this study, we reported a hierarchically structured PV nanomaterial based on upright-standing nanoporous nanosheets of iodine-doped ZnO nanocrystalline (denoted as ZnO:I) exhibiting higher conversion efficiency, large internal surface area as well as strong light scattering property, which can be used as an effective photoanode in DSSCs. The nanosheets were sub-micrometer-sized and thus can function as efficient light scatterers, whereas the nanocrystallites provide the films with the necessary nanoporous structure and large internal surface area. The proposed multifunctional ZnO:I nanosheets produced an efficiency of 6.6%, almost more than double of undoped ZnO nanosheets (2.4%), much higher than 0.5−1.5% for ZnO nanowires films,[13,14,31] 1.5−2.4% for ZnO nanocrystalline films,[32−34] and 2.7−3.5% for uniform ZnO aggregate films.[35] The enhancement effect was anticipated to be equally applicable to achieving a higher efficiency for other oxide semiconductor-base DSSCs.

2. EXPERIMENTAL SECTION

2.1. Synthesis of Nanoporous Nanosheets of ZnO and ZnO:I Nanocrystallites. In the two-step method, ZnO seed layers were deposited onto the heated fluorine-doped tin oxide (FTO) substrates by applying the electrostatic spray deposition method.[36] The preparation process and experimental conditions were similar to our previous report.[37]

In the second stage of deposition, nanoporous nanosheets of ZnO:I nanocrystallites were grown in a sealed reaction vessel via hydrothermal decomposition of hexamethylenetetramine (HMT) and zinc nitrate hexahydrate ($Zn(NO_3)_2{\cdot}6H_2O$) solutions based on a modified method.[38] An iodine(I) dopant was added in the form of iodic acid (HIO_3) with doping concentration of 2.2 at % into the equimolar solution of 0.01 M $Zn(NO_3)_2{\cdot}6H_2O$/HMT. The seeded substrates were suspended inside the sealed reaction vessel with 0.01 M of equimolar solution & I dopant and were heated to 50, 60, 70, and 80 °C, respectively, for the growth of sample 1 (upright-standing well-stacked nanoporous nanosheets of ZnO:I nanocrystallites synthesized at 50 °C), sample 2 (slight destruction of the standing nanosheets synthesized at 60 °C), sample 3 (partial nanosheets synthesized at 70 °C) and sample 4 (primary nanocrystallites without any nanoporous nanosheets synthesized at 80 °C). Another equimolar solution of 0.01 M $Zn(NO_3)_2{\cdot}6H_2O$/HMT was prepared without the addition of I dopant for growing the nanosheets of ZnO nanocrystallites. Similarly, the ZnO seeded substrates were suspended inside the sealed reaction vessel with 0.01 M of equimolar solution without I dopant and were heated to 50, 60, 70, and 80 °C, respectively for the growth of four different samples (sample 5 (at 50 °C), 6 (at 60 °C), 7 (at 70 °C), and 8 (at 80 °C)) of undoped ZnO nanosheet films. The FTO substrates containing eight different samples, were removed from vessel and washed with distilled water after 10 h of growth in order to remove the residual zinc salts and they were dried in a stream of air before further analysis. Unless mentioned, the synthesis temperature of 50 °C was kept constant and the solar cell performance was checked after zero days.

2.2. ZnO and ZnO:I Cell Preparation. Nanoporous nanosheets of ZnO and ZnO:I nanocrsytallites were washed with DI water and baked in air at 350 °C for 30 min in order to remove any residual organics and optimize solar cell performance. The nanosheets films were then sensitized by dipping them into 0.5 mM ethanolic solution of the ruthenium complex *cis*-$[RuL_2(NCS)_2]$ (commercially known as

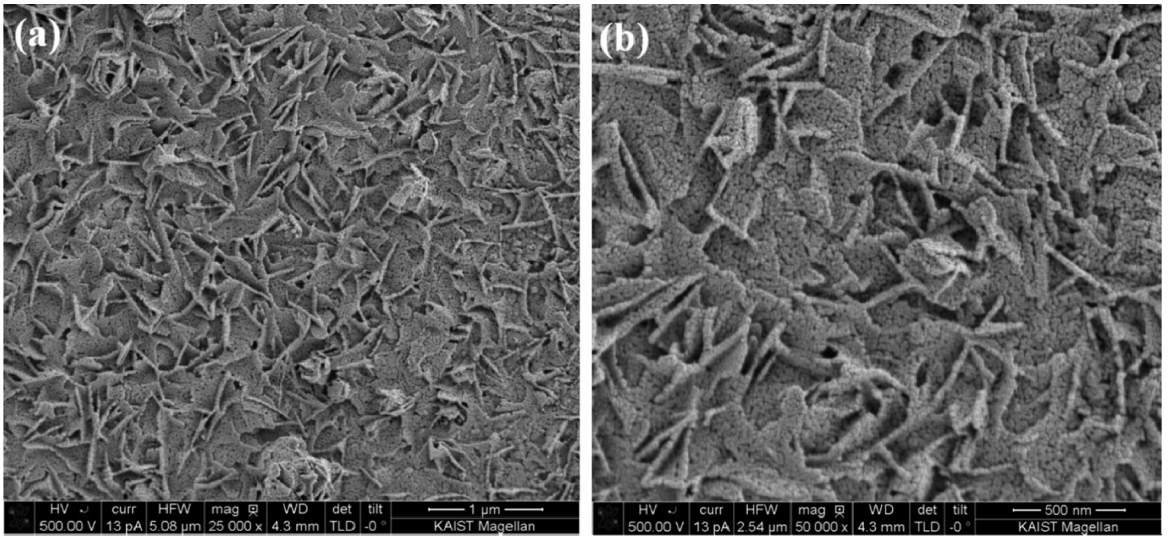

Figure 1. (a) FE-SEM image of as-prepared ZnO:I nanosheets (sample 1), and (b) a magnified FE-SEM image of nanosheets.

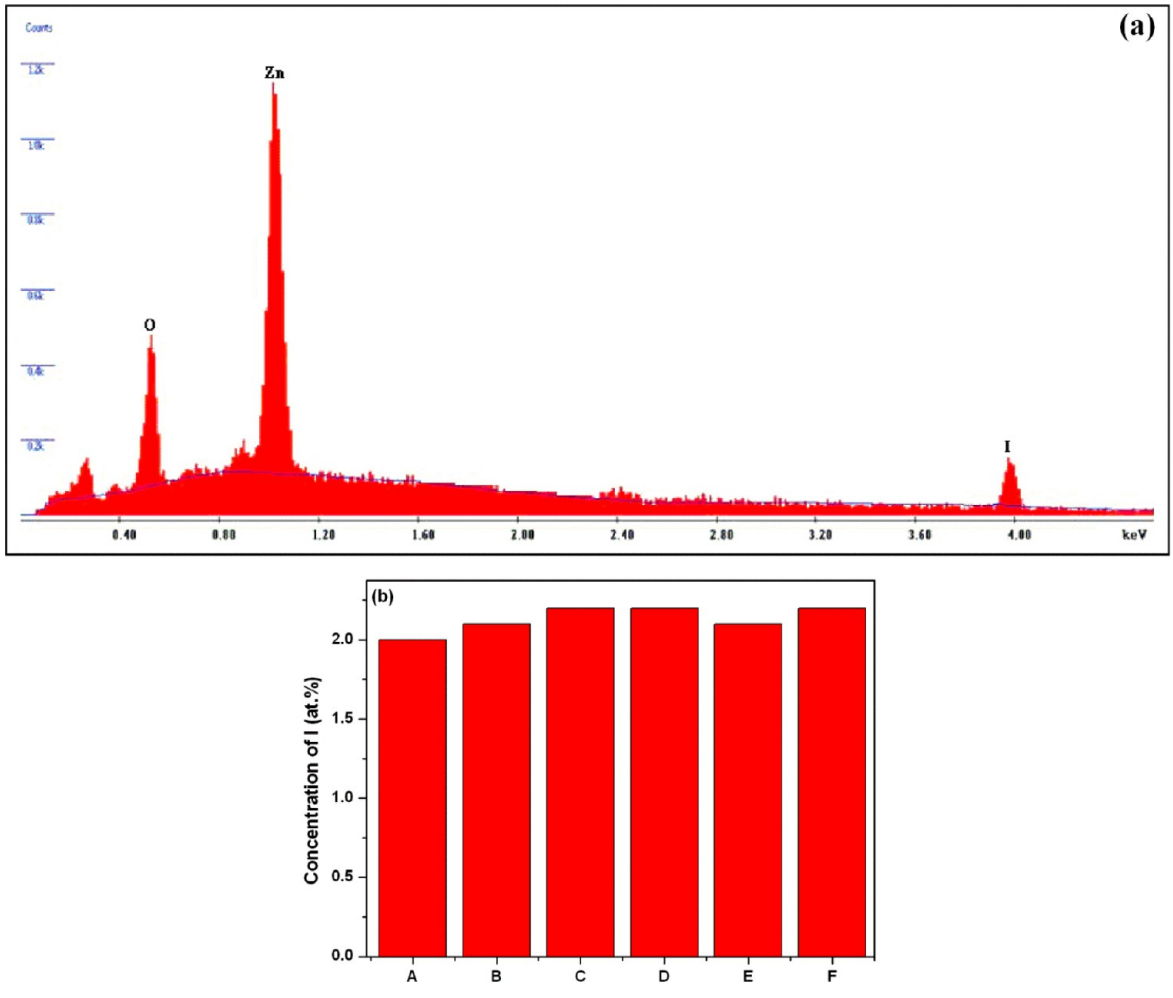

Figure 2. (a) EDS spectrum of ZnO:I nanosheet film (sample 1). Strong Zn peaks, as well as weak I atomic peaks at around 3.95 keV, were detected in the EDS spectrum, and (b) EDS results obtained by scanning nanosheets of ZnO:I nanocrystallites in different areas.

N3 dye) for approximately 30 min. The sensitization time was controlled strictly to avoid the dissolution of surface Zn atoms and the formation of Zn^{2+}/dye complexes, which might block the electron transport from the dye to the semiconductor. To remove the additional dye, we then washed the films of nanosheets with ethanol. The Pt-coated thin films on the FTO, which served as counter electrodes, were constructed by dropping 0.35 mM H_2PtCl_6 solution on the FTO, followed by annealing at 400 °C for 15 min in air. The electrolyte solution consisted of 0.3 M LiI, 0.06 M I_2, 0.5 M t-BPy, and 1.0 M DMPII in acetonitrile. The active area of the resulting cell

dx.doi.org/10.1021/am303272g | ACS Appl. Mater. Interfaces 2013, 5, 3075−3084

exposed in light was approximately 0.25 cm^2 (0.5 cm × 0.5 cm). For comparison, ZnO cell was also constructed according to a similar procedure as mentioned above.

2.3. Characterization. The crystal structure of the nanosheets films was analyzed by using an X-ray diffaractrometer (D/MAX-2500 Rigaku Co.) using Cu kα radiation (λ = 1.5405 Å). For the surface morphology of the nanosheets films, field-emission scanning electron microscopy (FE-SEM) was performed by using a Magellan 400 microscope coupled with an X-ray energy dispersive spectrometer (EDXS) DX-4, which further revealed the elementary composition of the nanosheets. The current density versus voltage (J−V) characteristics of the cells were measured using a solar simulator (Newport) and a black metal mask with an aperture area of 0.215 cm^2 under steady illumination AM1.5 spectral filter, and the intensity was adjusted to provide 1 sun (100 mW cm^{-2}) using a calibrated silicon solar cell. A 1000 W xenon lamp (Thermo Oriel, America) was served as the light source. Monochromatic light in the range of 400−800 nm was obtained by using a series of filters. The incident photo to current conversion efficiency (IPCE) was measured as a function of wavelength from 400 to 800 nm on a Keithley model 2000 SourceMeter under short circuit conditions using a tungsten source. The BET data of doped and undoped ZnO nanosheet-based samples was obtained with the help of an ASAP 2010 surface area analyzer. The amount of dye adsorbed on the photoanode was determined by measuring the absorption spectra of dye desorbed by immersing the photoanode into 1.0 M NaOH solution (50:50, V/V). The absorption spectra were measured using an ultraviolet visible-near-infrared (UV−vis−NIR) spectrophotometer (UV-3101PC), with an integrating sphere to capture directly the transmitted light and forward scattered light. The electrochemical impedance spectroscopy (EIS) measurements were performed by applying a bias of the open-circuit voltage of the ZnO and ZnO:I-based cells with AC amplitude of 10 mV and a frequency ranging from 1 × 10^{-1} to 1 × 10^5 Hz under 100 mW cm^{-2} illumination.

3. RESULTS AND DISCUSSION

The scanning electron microscopy (SEM) image (Figure 1a) indicates that the film was well stacked with nanoporous nanosheets of ZnO:I nanocrystallites with diameters ranging from several tens to several hundreds of nanometers (Figure 1b); the magnified SEM image of nanosheets of ZnO:I nanocrystallites reveals that the ZnO nanosheets consist of packed nanocrystallites. This ZnO:I film had a hierarchical structure, which stems from the combined architecture of the film formed by secondary nanosheets with primary nanocrystallites. The sample synthesized at 50 °C was denoted as sample 1, which also demonstrates the porous features provided by the nanosheets of nanosized crystallites. Energy-dispersive spectroscopy (EDS) measurement demonstrates the existence of I in ZnO nanosheets (Figure 2a). By scanning nanosheets of ZnO:I nanocrystallites in different areas, the average concentration of I was estimated to be ∼2.1 at % (Figure 2b). Similarly, the EDS and the estimation of average concentration I of was performed for all other ZnO:I nanosheet film samples. Those results revealed that I also exists in the nanosheet films.

Figure 3 exhibits the X-ray diffraction (XRD) pattern of the ZnO:I nanosheet films (sample 1) and pure ZnO nanosheet film (sample 5), where all the major peaks can be well assigned to those of wurtzite (hexagonal) ZnO with lattice constants of a = 0.325 nm and c = 0.521 nm (JCPDS: 36−1451). It was observed that the intensity of (0 0 2) peak was much stronger than that of other peaks, demonstrating that the (0 0 1) crystal face might be the primary face of the nanosheets. The inset of Figure 3 exhibits the comparison of the XRD pattern of iodine-doped and undoped ZnO nanosheets in the range 2θ = 31−37° corresponding to (1 0 0), (0 0 2), and (1 0 1) peaks. By

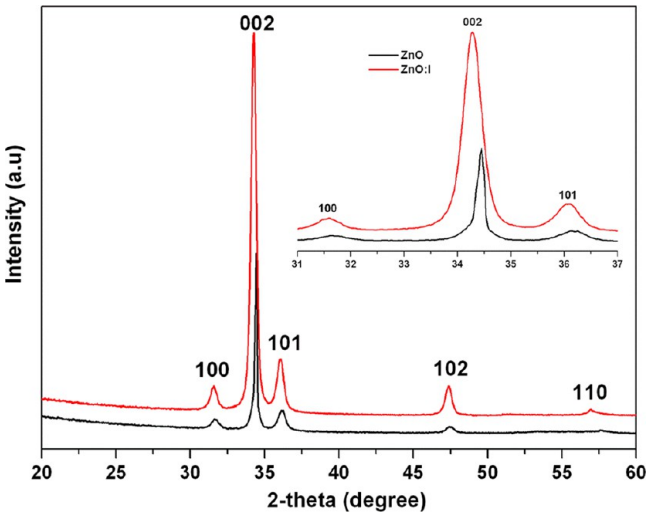

Figure 3. XRD patterns of iodine-doped and pure nanosheets of ZnO crystallites. The inset shows the XRD comparison of both samples showing the peak shifting because of the doping in the range 2θ = 31−37°.

observing the peak positions, it was observed that peaks had a slight shift toward the smaller angle side. The peak shift was resulted from the lattice expansion caused by doping. The evaluated c-axis lattice constant of the iodine-doped nanosheets was 0.5240 ± 0.0005 nm, which was much larger than that of pure ZnO (c = 0.5109 nm). These results demonstrated that I was successfully occupied into the ZnO lattice.

Additionally, three more ZnO:I nanosheets films (samples 2, 3, and 4) with various morphologies were fabricated at 60, 70, and 80 °C, respectively. Figure 4 shows the typical FE-SEM images of these three samples, explaining the steady depravity in the degree of upright-standing position of nanosheets of nanocrystallites by increasing synthesis temperature. Sample 2, synthesized at 60 °C, was similar to sample 1 and contained the nanoporous nanosheets of ZnO:I nanocrystallites, but sample 2 exhibited a slight degradation of the standing nanosheets (Figure 4a). Sample 3, which was synthesized at 70 °C (Figure 4b) contained only partial nanosheets. It was clear in sample 3, that most of the nanosheets had lost their standing position. When the temperature increased up to 80 °C, the obtained ZnO:I film (sample 4, Figure 4c) only exhibited the primary nanocrystallites without any nanoporous nanosheets. Moreover, XRD analysis demonstrated that all the four different ZnO:I films had the hexagonal wurtzite structure, despite the various morphologies and the synthesis temperatures. The primary nanocrystallite size, estimated from the full width at half-maximum of the (0 0 2) peak using the Scherrer equation revealed that the ZnO:I nanocrystallites were 25 nm in diameter, and there was no considerable difference in nanocrystallite size for all the samples regardless of the various morphologies observed by FE-SEM.

The ZnO:I nanosheet film (sample 1) of approximately ∼1.2 ± 0.3 μm in thickness was grown using a hydrothermal method onto a FTO coated glass at 50 °C as shown in Figure 5a. For comparison, undoped ZnO film of nanosheets (sample 5) with thickness of ∼1.2 ± 0.3 μm identical to that of the ZnO:I film was also grown, and it was examined that the two films maintained the analogous morphology and structure (Figure 5b and 5c). Moreover, for other undoped ZnO and ZnO:I samples

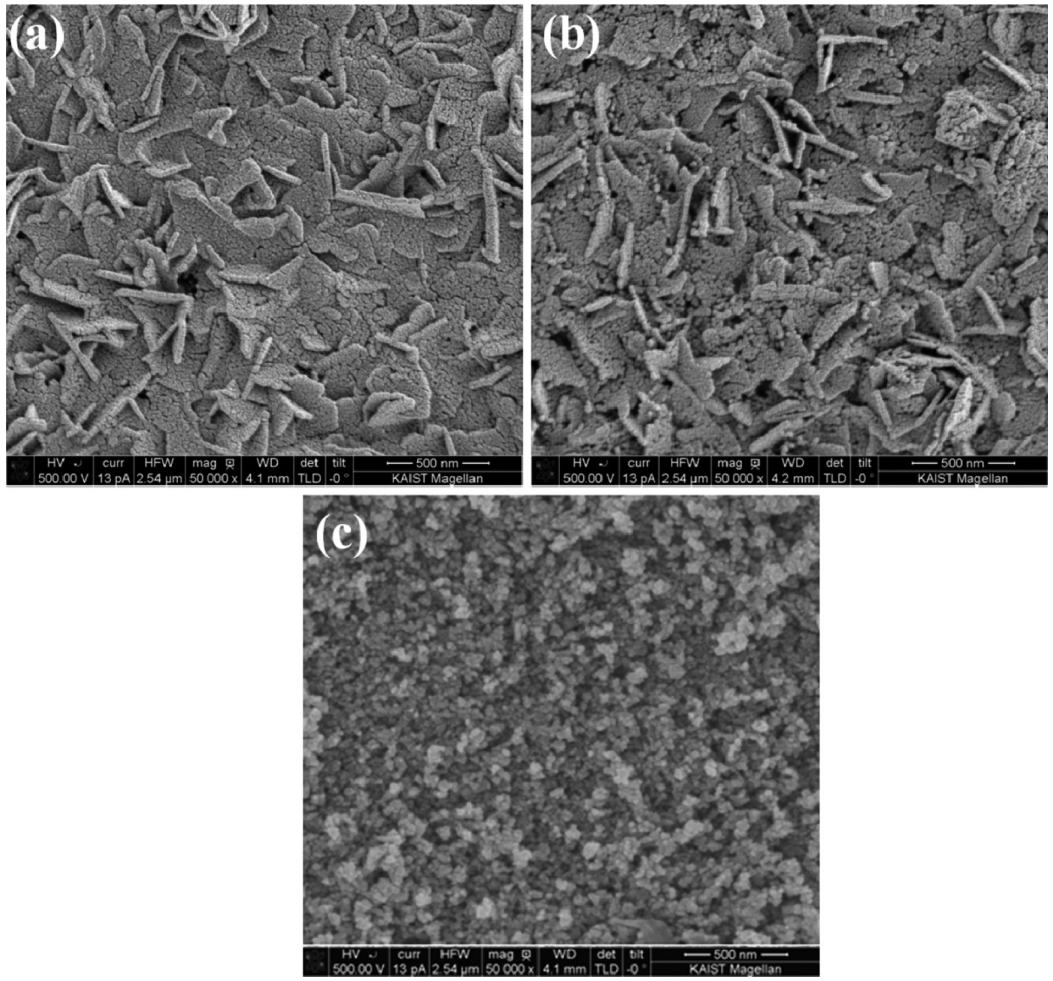

Figure 4. FE-SEM images presenting the morphology evolution of ZnO:I nanosheets films synthesized at different temperatures: (a) 60 °C (sample 2), (b) 70 °C (sample 3), and (c) 80 °C (sample 4).

the films of nanosheets had the same thickness of about ~1.2 ± 0.3 μm.

The fabricated solar cells based on ZnO:I and undoped ZnO nanosheet films were further identified by measuring their current−voltage behavior while the cells were irradiated by AM 1.5 simulated sunlight with a power density of 100 mW cm^{-2}. Figure 6 displays the typical current density versus voltage (J−V) curves of the four different ZnO: I samples and one undoped ZnO sample. In the case of undoped ZnO (sample 5) based cell, the short-circuit current density (J_{SC}) of 9.5 mA/cm^2, open-circuit voltage (V_{OC}) of 595 mV and energy-conversion efficiency (η) of 2.4% were obtained. After doping with iodine, the J_{SC} and η were enhanced significantly, reaching a maximum of up to 20.0 mA/cm^2 and 6.6%, respectively. The highest η of ZnO:I cell conformed to a more than 100% increment of undoped ZnO cell. Moreover, sample 1 that contains the near perfect up-right standing nanosheets structure, accomplished the highest J_{SC} and, thus, the highest η, whereas sample 4, composed of only ZnO nanocrystallites, showed the lowest current density and the lowest energy conversion efficiency among all four samples. Table 1 outlines the V_{OC}, J_{SC}, fill factors (FF), η, synthesis temperature, approximate film thickness, surface area and the amount of absorbed dye for all four different ZnO:I samples and an undoped ZnO sample. All samples revealed the similar open-circuit voltages of approximately 600 mV; but, the short-circuit current density was decreased significantly from 20 mA/cm^2 for sample 1 to 12.4 mA/cm^2 for sample 4. As a result, the energy conversion efficiency varied systematically from 6.6% for sample 1 to 3.2% for sample 4, decreasing as the degree of standing of nanosheets decreased. In a DSSC, the current density was decided based on the injection efficiency of electrons from dye molecules to semiconductor, the recombination rate between the injected electrons and oxidized dye or redox species in the electrolyte, and the initial number of photogenerated carriers. It was reasonable to assume the same injection efficiency and recombination rate for the given ZnO/N3/electrolyte systems, so that the initial number of photogenerated carriers may be significantly affected by the variation in the light-harvesting capability of photoelectrodes with different film structures. Thus, the enhanced performance of ZnO:I cells can be reasonably believed to be arising from the sunlight harvesting, photon-to-electron transfer process of the cells, as well as the intrinsic components of the films. The dye loading of the films was measured to investigate the surface concentration of dye molecules adsorbed on ZnO:I and undoped ZnO nanosheet films. The results showed a slight decrease in the surface concentration, with the values of 6.36 × 10^{-8}, 6.1 × 10^{-8}, 5.5 × 10^{-8}, and 4.3 × 10^{-8} molcm^{-2} for the samples 1−4, respectively, when the film morphology had alteration gradually from standing nanosheets to nanocrystallites, which may have different capability for dye

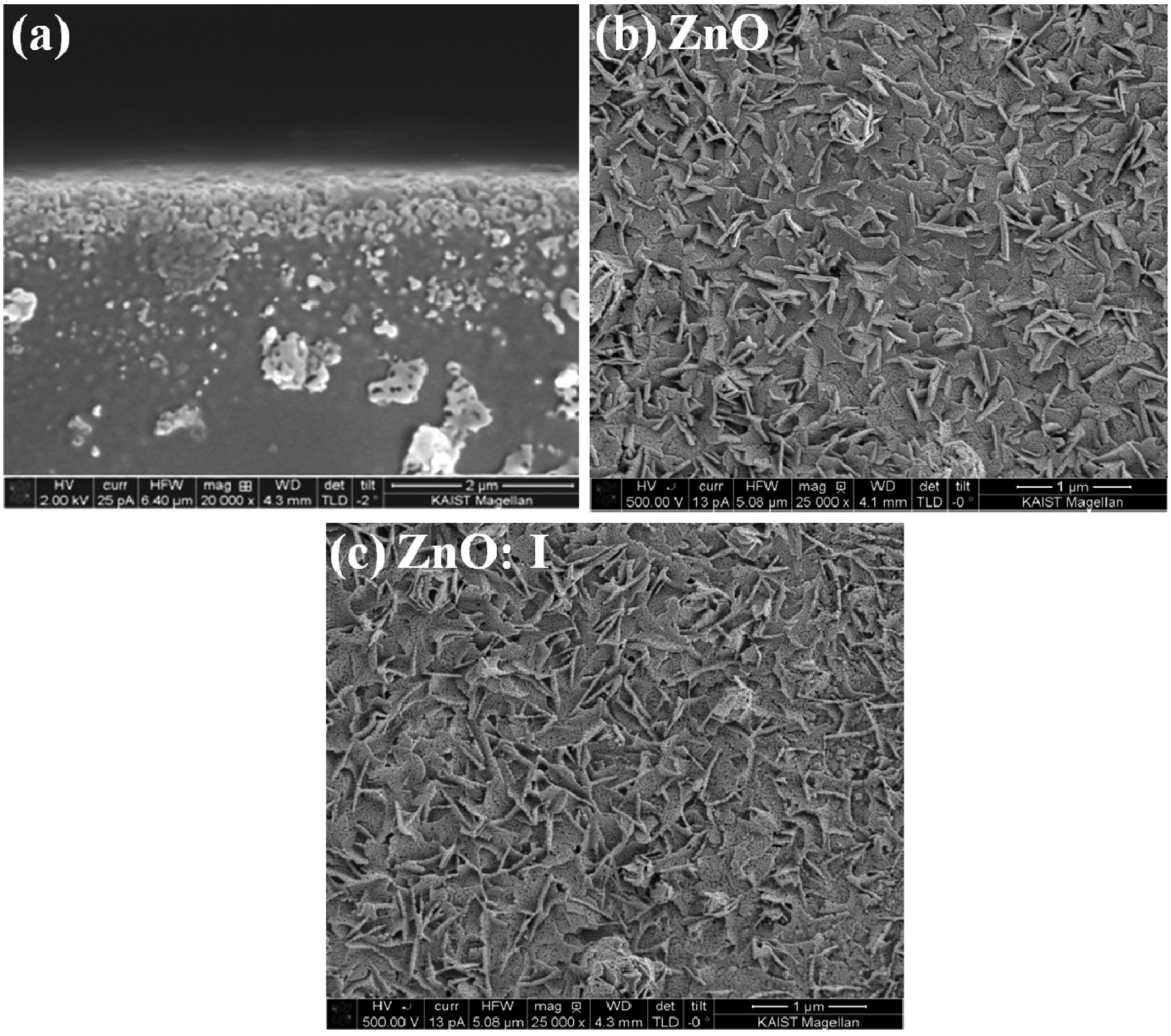

Figure 5. (a) Typical cross-sectional FE-SEM image of the ZnO: I film, showing approximately 1.2 ± 0.3 μm in thickness; FE-SEM image of (b) ZnO (sample 5), and (c) ZnO:I nanosheets films (sample 1). Both the ZnO-based films were stacked with nanoporous nanosheets of ZnO nanocrystalline particles.

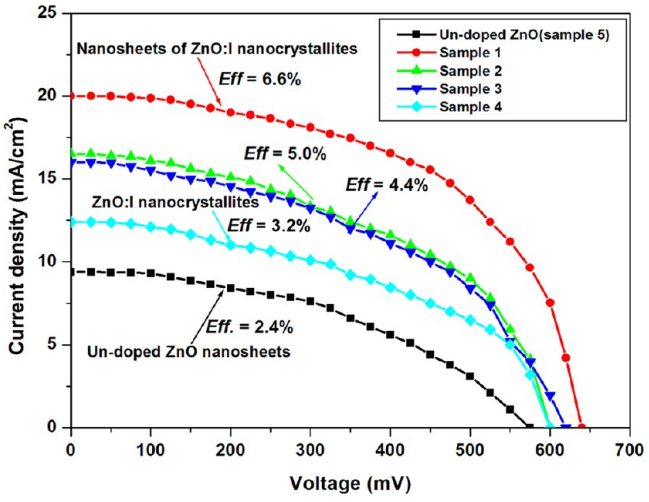

Figure 6. A comparison of photovoltaic behaviors of undoped ZnO and ZnO:I samples 1−4.

adsorption and therefore, a different porosity. In addition, all four different samples of ZnO:I exhibited a specific surface area of 75 ± 2 m^2 g^{-1}. Similar trend was observed in undoped ZnO nanosheet films with the values of 6.2 × 10^{-8}, 5.8 × 10^{-8}, 5.0 × 10^{-8}, and 3.7 × 10^{-8} molcm^{-2} for samples 5−8, respectively, when the change in the film morphology was observed from upright-standing nanosheets to nanocrystallites formation. On the other hand, it was also observed that the amount of dye absorbed in the films before (6.2 × 10^{-8} mol cm^{-2}) and after iodine doping (6.36 × 10^{-8} mol cm^{-2}) was almost identical, which was in good agreement with their analogous BET data (74.0 and 76 m^2 g^{-1} for undoped ZnO and ZnO:I, respectively) as well as film texture framework.

To investigate the reasons behind the higher photocurrent resulted from ZnO:I-based solar cells, we also performed the incident photon to current conversion efficiency (IPCE) for the ZnO:I and undoped ZnO cells to investigate the photoactive wavelength regime (Figure 7a). Particularly, the IPCE spectra of the ZnO:I film-based cells exhibited a red shift, promoting the employment of sunlight in the full spectrum range. The maxima of IPCE in the visible region committed by the dye absorption were situated at approximately 520 nm with values of 78, 73, 68, and 58% for samples 1−4, respectively. Hence, the IPCE measured for the sample 1 film with standing nanosheets was almost 1.35 times that of the sample 4 films with only nanocrystallites. Furthermore, IPCE examined for

Table 1. Summary of the Photovoltaic Characteristics for the Undoped ZnO and ZnO:I-Based Dye-Sensitized Solar Cells[a]

samples	synthesis temperature (°C)	film thickness (μm)	V_{OC} (mV)	J_{SC} (mA/cm^2)	FF (%)	η (%)	surface area (m^{2}g^{-1})	absorbed dye ($\times 10^{-8}$ mol cm^{-2})
undoped ZnO	50	1.2 ± 0.3	595 ± 3	09.5 ± 0.2(09.4)	42.4 ± 0.2	2.4 ± 0.2	74 ± 2	6.20 ± 0.2
1	50	1.2 ± 0.3	640 ± 2	20.0 ± 0.1(19.9)	51.7 ± 0.2	6.6 ± 0.1	76 ± 2	6.36 ± 0.2
2	60	1.2 ± 0.2	610 ± 2	16.5 ± 0.2(16.3)	49.6 ± 0.2	5.0 ± 0.2	75 ± 1	6.10 ± 0.1
3	70	1.2 ± 0.3	620 ± 1	16.0 ± 0.3(15.8)	44.3 ± 0.2	4.4 ± 0.2	75 ± 1	5.50 ± 0.3
4	80	1.2 ± 0.3	605 ± 2	12.4 ± 0.2(12.3)	42.1 ± 0.2	3.2 ± 0.2	75 ± 1	4.30 ± 0.1

[a]Average performance (mean values) has been calculated for 10 devices. J_{SC} values in brackets were calculated from IPCE.

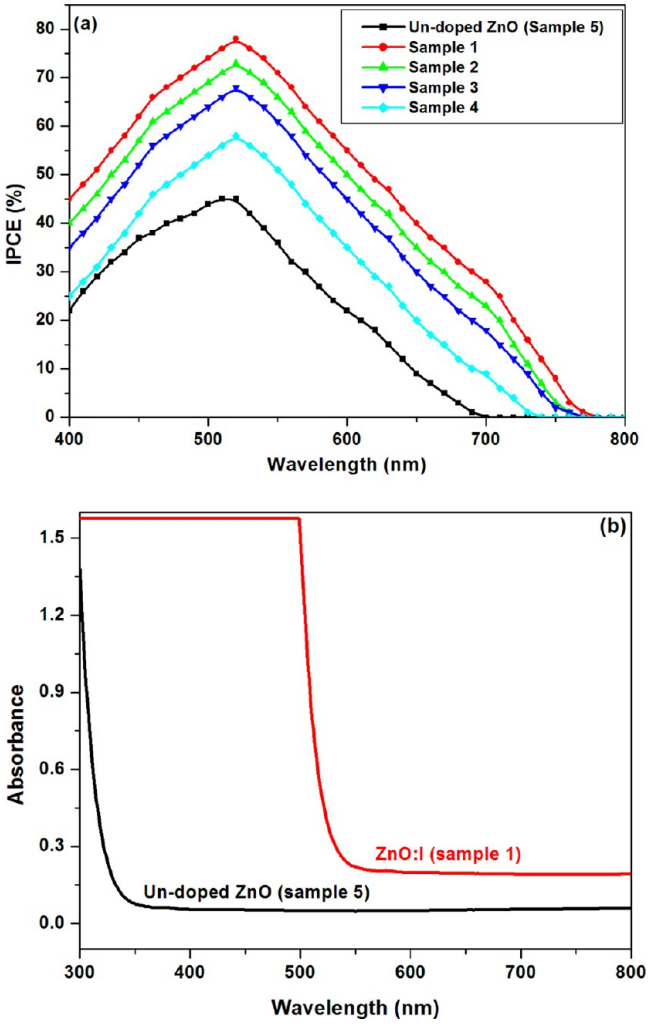

Figure 7. (a) Comparison of IPCE spectra of undoped ZnO (sample 5) and ZnO:I samples 1−4 measured in DC mode, and (b) absorption spectra of undoped ZnO and ZnO: I films, exhibiting that the presence of I dopant successfully induces the red-shift of the nanocrystalline absorption.

sample 1 was almost 1.75 times higher than undoped ZnO sample. Optical absorption spectra for ZnO:I and undoped ZnO films with dye sensitization revealed the difference in light-harvesting capabilities of the films. The red shift was also examined in UV−vis absorption spectroscopy measurements (Figure 7b). Also, IPCE profile of ZnO:I cell was found to be broadened and strengthened over the entire wavelength region compared to that of undoped ZnO cell. The absorption spectra demonstrates that the ZnO nanosheet films with better standing position can promote more efficient photon capturing in the visible region and also suggest the existence of a strong light scattering effect. In addition, such an effect might be helpful for the partial scattering of the incident light and weaken the transmittance of the films, and thus produces the pseudo-absorption deviating from that of adsorbed dye.

In the DC mode, the photocurrent was measured under the illumination of monochromatic light with a fixed photon flux which is normally 10^{14} cm^{-2} s^{-1}. The generated photocurrent may be 3 orders of magnitude smaller than that generated under AM 1.5G solar light. Therefore, it was hard to measure the IPCE of DSSCs precisely with such small photon flux, so the photon flux of the monochromatic light was increased to 1×10^{16} cm^{-2} s^{-1}.[39] Figure 8a exhibits the IPCE spectra of a ZnO:I (sample 1) based DSC measured under the AC mode (2 Hz) and the DC mode with fixed photon flux of 1×10^{16} cm^{-2} s^{-1}, respectively. In the range of 600 to 900 nm, the IPCE values of the two modes were very close to each other. The same trend was observed for other samples.

In addition, it is crucial to justify that the J_{SC} obtained from $J-V$ measurement was compatible with the value estimated from IPCE spectra, because J_{SC} can be expressed by integrating the product of the incident photon flux density [F(λ)] and IPCE (λ) of the cell over the wavelength (λ) of the incident light, expressed as[40]

$$J_{SC} = \int qF(\lambda)(1 - r(\lambda))\mathrm{IPCE}(\lambda)d\lambda \quad (1)$$

where q is the electron charge and r(λ) the incident light loss in light absorption and reflection by the conducting glass.

Figure 8b demonstrates the relationship between J_{SC} calculated from eq 1 and J_{SC} measured from $J-V$ characteristics (Figure 6), for an undoped ZnO (sample 5) and ZnO:I samples 1−4 at 700 nm. In the calculation, [F(λ)] was assumed to be AM 1.5 standard spectrum. A linear relationship was obtained between the calculated and measure J_{SC}. The slope of the line was close to 1, suggesting that IPCE could be accurately measured under DC mode, which revealed that the IPCE spectra measured in the DC mode could be reliable if the measurement conditions were properly analyzed. The DC mode would only be valid when J_{SC} has a linear relationship as a function of light intensity. However, for DSSCs with a nonlinear relationship, such as the DSSCs based on ionic liquids, the DC mode was not reliable anymore.[41,42] Hence, we also measured the IPCE spectrum in the AC mode at a frequency low enough for the illumination of simulated solar light.

To obtain the information about the recombination properties and electron transport for ZnO:I cells, we measured the electrochemical impedance spectroscopy (EIS) (Figure 9) at an applied bias of V_{OC} under illumination. The Nyquist plots (see the inset of Figure 9) showed a well-defined semicircle in the low-frequency region (100−1 Hz) resulting from electron

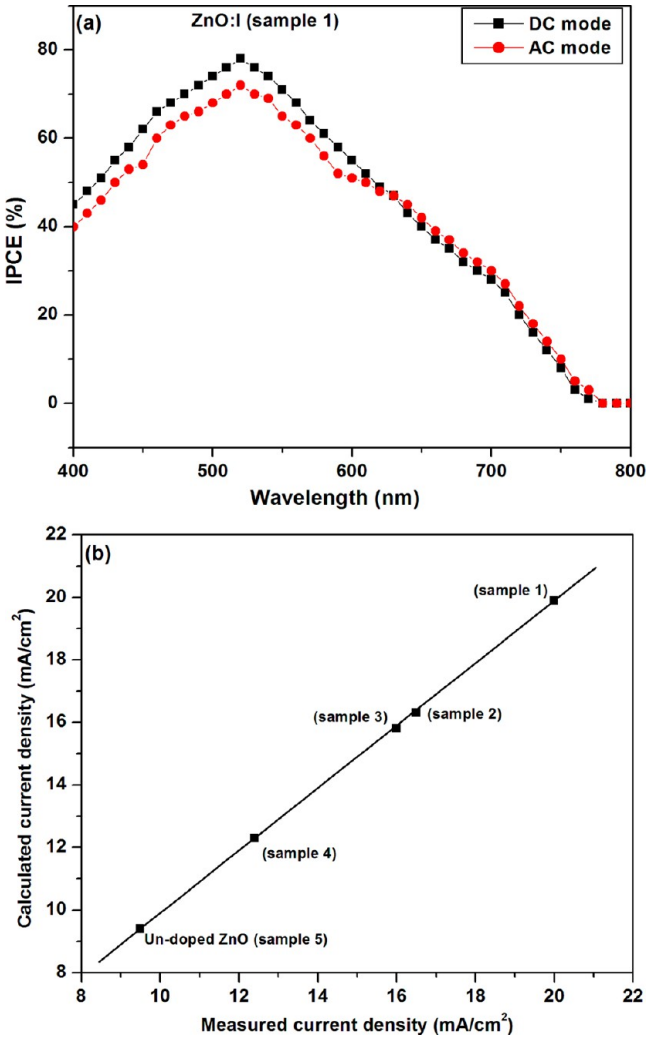

Figure 8. Comparison of IPCE spectra of ZnO:I (sample 1) measured under AC mode with AM 1.5 simulated sunlight and DC mode without simulated sunlight, (b) Relationship between J_{SC} calculated from eq 1 and J_{SC} measured from $J-V$ characteristics for an undoped ZnO (sample 5) and ZnO:I samples 1–4.

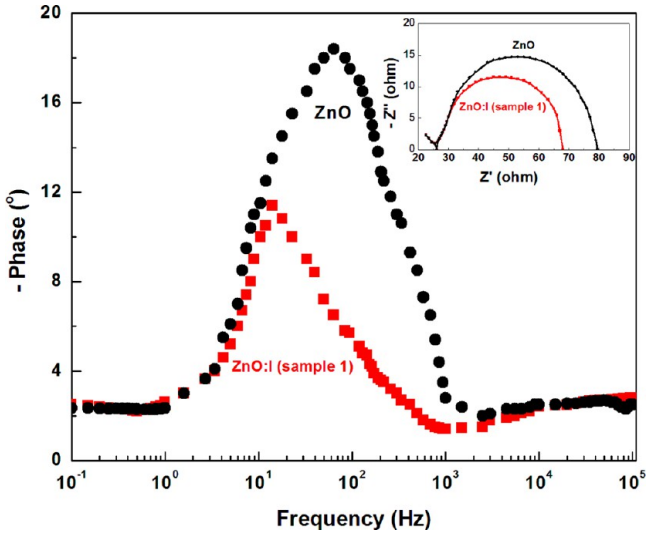

Figure 9. Bode phase plots of undoped ZnO (sample 5) and ZnO:I (sample 1)-based DSSCs measured at the V_{oc} under 100 mW cm^{-2} illumination. The inset displays the Nyquist plots of the corresponding two cells.

transfer at the ZnO/dye/electrolyte interface which governs the impedance of the DSSC, and was recognized as the characteristic shape of recombination through the semiconductor.[8] No current passes through the external circuit under the V_{OC} condition and the injected electrons into the ZnO or ZnO:I must be recombined by redox electrolyte at the ZnO/dye/electrolyte interface. The electron lifetime (τ_e) in the ZnO-based films can be obtained from the maximum frequency of the low-frequency peak (f_{max}) value following the equation $\tau_e = 1/\omega_{max} = 1/2\pi f_{max}$.[43−45]

Bode phase plots (Figure 9) demonstrated that I doping in ZnO leads to a decrease in the f_{max} values, and τ_e was found to be 4.5 and 11.8 ms for ZnO and ZnO:I cells, respectively which demonstrated that the transfer of electrons over a longer distance was unblocked to a larger span across the ZnO:I/dye/electrolyte interface, directing to a larger collection of electrons and effective capture. In addition, the decrease in charge recombination and the increase in τ_e which was observed for ZnO:I cell, could be the consequence of I doping, that acts as charge trapping site for the separation of electron−hole, and therefore, contributes to the enhancement of photon-to-electron conversion efficiency.[9,43−46]

Another impressive perspective of the ZnO-based DSSC system is its high durability of the device performance compared to other liquid junction solar cells. Practically, the liquid junction solar cells are known to have the low stability originated from the leakage currents, corrosion of quantum dots and side reactions at the electrolyte/counter electrode interface. In view of stability, ZnO-based DSSCs is advantageous due to its ability to work at wider angles, robustness to corrosion, capability to operate at lower internal temperatures, mechanically robustness, air stability, and nonvolatility. Figure 10 shows the cell performance durability for 35 days. The undoped ZnO and ZnO:I nanosheet-based cell performance was measured every 7 days in the presence of air, and the results exhibited that it was not degraded even after 35 days. The dependence of the current density, open circuit voltage, fill factor and the overall conversion efficiency on time durations showed a decrease by only ∼5−6% even after 35 days. This high stability for cell performances of our ZnO and ZnO:I nanosheet-based DSSCs has a great potential as a next-generation solar cell.

4. CONCLUSIONS

In conclusion, the upright-standing nanoporous nanosheets of undoped ZnO and ZnO:I nanocrystallites have been demonstrated as an effective approach to generate light scattering within the photoelectrode film of DSSCs while retaining the desired specific surface area for dye-molecule adsorption. The maximum energy conversion efficiency of 6.6% was achieved on photoelectrode films that consisted of well stacked up-right standing nanosheets of ZnO: I nanocrystallites. This efficiency is enhanced more than 100% over the 2.4% achieved for undoped ZnO films. In addition, IPCE spectra of ZnO:I cell exhibited a significant enhancement in light harvesting, especially in the visible region. Therefore, ZnO:I may be developed as a promising photoelectrode material for high-efficiency DSSCs. EIS data and analysis results further proved that I doping lowered the recombination resistance and

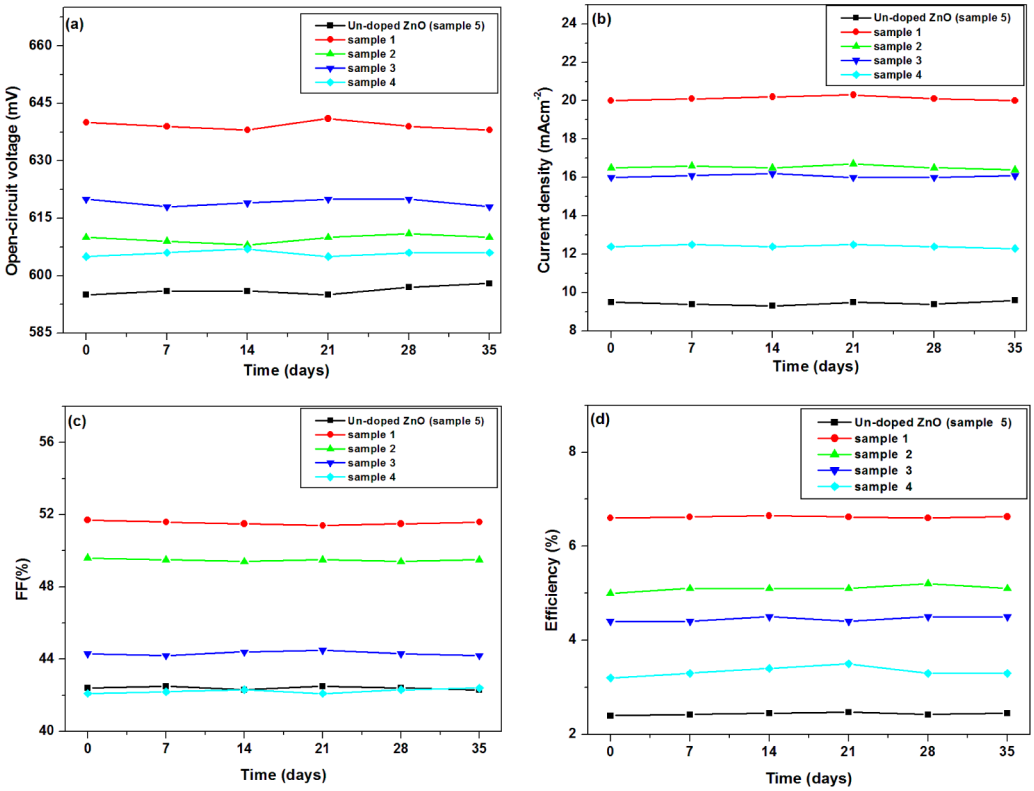

Figure 10. (a) Open-circuit voltage, (b) current density (c) fill factor, and (c) cell efficiency as a function of time for the stability test of the undoped ZnO and ZnO:I nanosheet films based-device stored for 35 days in air under ambient conditions.

prolonged electron lifetime of the ZnO:I nanosheet films, therefore diminishing the recombination process. The fabricated cell showed remarkable durability in cell performance; the cell efficiency decreased by only a few percent in air over 35 days. The proposed growth process is a simple and low-cost approach for the large scale production of nanomaterials with high conversion efficiency to fabricate DSSCs and hybrid solar cells. This method is also anticipated to be equally applicable to other semiconductor photoelectrodes in DSSCs and organic−inorganic hybrid solar cells.

AUTHOR INFORMATION

Corresponding Author

*Tel:+82-42-350-3298. Fax: +82-42-350-3910 E-mail address: SeungBinPark@kaist.ac.kr.

Notes

The authors declare no competing financial interest.

ACKNOWLEDGMENTS

This work was supported by the National Research Foundation of Korea (NRF) grant funded by the Korea government (MEST) (2010-0027634).

REFERENCES

(1) Xu, H.; Tao, X.; Wang, D.-T.; Zheng, Y.-Z.; Chen, J.-F. *Electrochim. Acta* **2010**, *55*, 2280.
(2) Anta, J. A.; Guillen, E.; Tena-Zaera, R. *J. Phys. Chem. C* **2012**, *116*, 11413−11415.
(3) Yella, A.; Lee, H.-W.; Tsao, H. N.; Yi, C.; Chandiran, A. K.; Nazeeruddin, M. K.; Diau, E. W.-G.; Yeh, C.-Y.; Zakeeruddin, S. M.; Gřatzel, M. *Science* **2011**, *334*, 629−634.
(4) Guo, M.; Diao, P.; Cai, S. *Chin. Chem. Lett.* **2004**, *15*, 1113.
(5) Guo, M.; Diao, P.; Wang, X.; Cai, S. *J. Solid State Chem.* **2005**, *178*, 3210.
(6) Gao, Y.; Nagai, M.; Chang, T.-C.; Shyue, J.-J. *Cryst. Growth Des.* **2007**, *7*, 2467.
(7) Wang, K.; Chen, J.; Zhou, W.; Zhang, Y.; Yan, Y.; Pern, J.; Mascarenhas, A. *Adv. Mater.* **2008**, *20*, 3248.
(8) Qian, J.; Liu, P.; Xiao, Y.; Jiang, Y.; Cao, Y.; Ai, X.; Yang, H. *Adv. Mater.* **2009**, *21*, 3663.
(9) Zhang, Q.; Dandeneau, C. S.; Zhou, X.; Cao, G. *Adv. Mater.* **2009**, *21*, 4087.
(10) Rensmo, H.; Keis, K.; Lindstrom, H.; Sodergren, S.; Solbrand, A.; Hagfeldt, A.; Lindquist, S. E.; Wang, L.; Muhammed, M. *J. Phys. Chem. B* **1997**, *101*, 2598.
(11) Yang, Z.; Xu, T.; Ito, Y.; Welp, U.; Kwok, W. K. *J. Phys. Chem. C* **2009**, *113*, 20521.
(12) Gřatzel, M. *Inorg. Chem.* **2005**, *44*, 6841.
(13) Law, M.; Greene, L. E.; Johnson, J. C.; Saykally, R.; Yang, P. D. *Nat. Mater.* **2005**, *4*, 455.
(14) Baxter, J. B.; Aydil, E. S. *Appl. Phys. Lett.* **2005**, *86*, 053114.
(15) Paulose, M.; Shankar, K.; Varghese, O. K.; Mor, G. K.; Grimes, C. A. *J. Phys. D: Appl. Phys.* **2006**, *39*, 2498.
(16) Wang, H.; Yip, C. T.; Cheung, K. Y.; Djurisic, A. B.; Xie, M. H.; Leung, Y. H.; Chan, W. K. *Appl. Phys. Lett.* **2006**, *89*, 023508.
(17) Nazeeruddin, M. K.; Kay, A.; Rodicio, I.; Humphry-Baker, R.; Mueller, E.; Liska, P.; Vlachopoulos, N.; Gřatzel, M. *J. Am. Chem. Soc.* **1993**, *115*, 6382.
(18) Gřatzel, M. *Nature* **2001**, *414*, 338.
(19) Zhang, Q.; Chou, T. P.; Russo, B.; Jenekhe, S. A.; Cao, G. *Angew. Chem., Int. Ed.* **2008**, *47*, 2402−2406.
(20) Memarian, N.; Concina, I.; Braga, A.; Rozati, S. M.; Vomiero, A.; Sberveglieri, G. *Angew. Chem., Int. Ed.* **2011**, *50*, 12321−12325.
(21) Guillen, E.; Azaceta, E.; Peter, L. M.; Zukal, A.; Tena-Zaera, R.; Anta, J. A. *Energy Environ. Sci.* **2011**, *4*, 3400−3407.
(22) Hosono, E.; Mitsui, Y.; Zhou, H. *Dalton Trans.* **2008**, *40*, 5439−5441.

(23) Lai, Y. H.; Lin, C. Y.; Chen, H. W.; Chen, J. G.; Kung, C. W.; Vittal, R.; Ho, K. C. *J. Mater. Chem.* **2010**, *20*, 9379−9385.
(24) Kakiuchi, K.; Hosono, E.; Fujihara, S. *J. Photochem. Photobiol. A* **2006**, *179*, 81−86.
(25) Suliman, A. E.; Tang, Y. W.; Xu, L. *Sol. Energy Mater. Sol. Cells* **2007**, *91*, 1658−1662.
(26) Akhtar, M. S.; Khan, M. A.; Jeon, M. S.; Yang, O. B. *Electrochim. Acta* **2008**, *53*, 7869−7874.
(27) Hosono, E.; Fujihara, S.; Honma, I.; Zhou, H. *Adv. Mater.* **2005**, *17*, 2091−2094.
(28) Xu, F.; Dai, M.; Lu, Y. N.; Sun, L. T. *J. Phys. Chem. C* **2010**, *114*, 2776−2782.
(29) Yang, X.; Wolcott, A.; Wang, G.; Sobo, A.; Fitzmorris, R. C.; Qian, F.; Zhang, J. Z.; Li, Y. *Nano Lett.* **2009**, *9*, 2331.
(30) Chen, L.-C.; Tu, Y.-J.; Wang, Y.-S.; Kan, R.-S.; Huang, C.-M. *J. Phptochem. Photobiol. A: Chem.* **2008**, *199*, 170.
(31) Du-Pasquier, A.; Chen, H. H.; Lu, Y. C. *Appl. Phys. Lett.* **2006**, *89*, 253513.
(32) Otsuka, A.; Funabiki, K.; Sugiyama, N.; Yoshida, T. *Chem. Lett.* **2006**, *35*, 666.
(33) Zeng, L. Y.; Dai, S. Y.; Xu, W. W.; Wang, K. J. *Plasma Sci. Technol.* **2006**, *8*, 172.
(34) Lee, W. J.; Suzuki, A.; Imaeda, K.; Okada, H.; Wakahara, A.; Yoshida, A. *Jpn. J. Appl. Phys. Part1* **2004**, *43*, 152.
(35) Chou, T. P.; Zhang, Q.; Fryxell, G. E.; Cao, G. *Adv. Mater.* **2007**, *19*, 2588.
(36) Li, J.; Fan, H. Q.; Jia, X. H.; Chen, J.; Cao, Z. Y.; Chen, X. P. *J. Alloys Compd.* **2009**, *481*, 735−739.
(37) Mahmood, K.; Park, S. B. *J. Cryst. Growth* **2012**, *347*, 104−112.
(38) Vayssieres, L. *Adv. Mater.* **2003**, *15*, 464−466.
(39) Yang, X.; Yanagida, M.; Han, L. *Energy Environ. Sci.* **2013**, *6*, 54−66.
(40) Chiba, Y.; Islam, A.; Watanebe, Y.; Komiya, R.; Koide, N.; Han, L. *Jpn. J. Appl. Phys.* **2006**, *45*, L638−L640.
(41) Moon, S.-J.; Yum, J.-H.; Humphry-Baker, R.; Karlsson, K. M; Hagberg, D. P.; Marinado, T.; Hagfeldt, A.; Sun, L.; Gr̈atzel, M.; Nazeeruddin, M. K. *J. Phys. Chem. C* **2009**, *113*, 16816−16820.
(42) Moon, S.-J.; Itzhaik, Y.; Yum, J.-H.; Zakeeruddin, S. M.; Hodes, G.; Grätzel, M. *J. Phys. Chem. Lett.* **2010**, *1*, 1524−1527.
(43) Lagemaat, J.; Park, N.-G.; Frank, A. J. *J. Phys. Chem. B* **2000**, *104*, 2044.
(44) Papageorgiou, N.; Maier, W. F.; Gr̈atzel, M. *J. Electrochem. Soc.* **1997**, *144*, 876.
(45) Wang, H.; He, J.; Boschloo, G.; Lindström, H.; Hagfeldt, A.; Lindquist, S.-E. *J. Phys. Chem. B* **2001**, *105*, 2529.
(46) Zhao, D.; Chen, C.; Wang, Y.; Ji, H.; Ma, W.; Zang, L.; Zhao, J. *J. Phys. Chem. C* **2008**, *112*, 5993.